Sonocrystallization of CMONS Needles and Nanocubes: Mechanistic Studies and Advanced Crystallinity Characterization by Combining X-ray and Electron Diffractions with DNP-Enhanced NMR

X. Cattoen, Akshay Kumar, Carole Vaillant, Mauricio Matta-Seclén, Fabien Dubois, Olivier Leynaud, Stéphanie Kodjikian, Sabine Hediger, Gaël de Paëpe, Alain Ibanez

To cite this version:

X. Cattoen, Akshay Kumar, Carole Vaillant, Mauricio Matta-Seclén, Fabien Dubois, et al.. Sonocrystallization of CMONS Needles and Nanocubes: Mechanistic Studies and Advanced Crystallinity Characterization by Combining X-ray and Electron Diffractions with DNP-Enhanced NMR. Crystal Growth & Design, 2022, 22 (4), pp.2181-2191. 10.1021/acs.cgd.1c01246 . hal-03619683

HAL Id: hal-03619683
https://hal.science/hal-03619683v1

Submitted on 25 Mar 2022

Sonocrystallization of CMONS needles and nanocubes: mechanistic studies and advanced crystallinity characterizations by combining X-ray and electron diffractions with DNP-enhanced NMR.

Xavier Cattoën,[†,*] *Akshay Kumar,*[‡] *Carole Vaillant,*[†] *Mauricio Matta-Seclén,*[†] *Fabien Dubois,*[†] *Olivier Leynaud*[†] *Stéphanie Kodjikian*[†] *Sabine Hediger*[‡] *Gaël de Paëpe,*[‡,*] *and Alain Ibanez*[†]

[†] Univ. Grenoble Alpes, CNRS, Grenoble INP, Institut Néel, 38000 Grenoble, France

[‡] Univ. Grenoble Alpes, CEA, CNRS, IRIG-MEM, Grenoble, France

AUTHOR INFORMATION

Corresponding Authors

Xavier Cattoën: Xavier.cattoen@neel.cnrs.fr

Gaël de Paëpe: gael.depaepe@cea.fr

KEYWORDS Sonocrystallization; Organic Nanocrystals; DNP-NMR; Fluorescence; Nanocrystallization.

ABSTRACT This study introduces a new nanocrystallization method assisted by ultrasounds that produces needles or nanocubes of CMONS, a stilbene dye, with an excellent control over the polymorphism, and with a narrow size distribution. Owing to the production of radicals from dissolved dioxygen by high-intensity ultrasounds, *trans*-to-*cis* isomerization was observed in the absence of nitrogen bubbling, with the formation of two distinct crystalline phases for the different diastereomers. The crystallinity of CMONS needles was probed by various techniques, including X-ray and electron diffractions, fluorescence spectroscopy, and dynamic nuclear polarization (DNP) enhanced solid-state nuclear magnetic resonance. The latter was used to hyperpolarize ^{1}H nuclei and to record ^{1}H-^{13}C and ^{1}H-^{15}N CPMAS NMR spectra at natural isotopic abundance with very high signal-to-noise ratio. With such sensitivity, one can easily discriminate between *cis* and *trans-I* forms of CMONS, detect the presence of multiple polymorphic phases (even with minor contributions) and check the absence of amorphous phase. Finally, the mechanism involved in the formation of CMONS needles was ascertained after stabilizing intermediate nanocubes against Ostwald ripening and ordered aggregation mechanisms using the CTAB surfactant.

Introduction

Organic nanocrystals (NCs) are being widely investigated owing to their wide range of applications,[1] since their first preparations as colloids, [2,3] embedded in sol-gel matrices [4] or formed within large pores-materials.[5] Nanosized drugs, amorphous or not, display faster solubilization than the bulk thanks to the increased surface to volume ratio, as exemplified by the widely used anti-cancer drug Doxil®.[6,7] Other applications of NCs include sensing,[8] organic electronics[9] and optical power limiters.[10] Nanosized organic dyes are also being intensively studied for application as tracers for *in vivo* fluorescence imaging.[11–16] In particular, the advent of aggregation-induced emission (AIE) has enabled the development of numerous nanoparticles (NPs) obtained by precipitation of a dye solution into water.[17–19] However, the fluorescence properties of the obtained colloids strongly depend on the ordering of the molecular packing and eventually on the polymorph that is formed when the NPs are crystalline. In particular, lots of AIE dyes-based NPs rely on *J*-aggregates, for which an ordered molecular assembly favors fluorescence emission. However, the structural characterization of molecular colloids is very delicate, which constitutes a strong limiting factor in many studies of fluorescent NPs and AIE fluorophores. Furthermore, some colloids were characterized after freeze-drying, but it has been shown that the freeze-drying process may itself provoke the crystallization of the dye.[11]

To prepare NCs colloids, the reprecipitation method[2] has been previously developed. It consists in injecting a solution of the compound to crystallize in a water-miscible solvent into water. However, this technique may lead to polydisperse mixtures as the time at which the critical supersaturation is reached, corresponding to the nucleation threshold, strongly depends on the solubility of the compound in the considered solvent. Furthermore, amorphous or ill-crystallized nanoprecipitates are often obtained,[14] while size and size distribution of molecular NPs are often difficult to master. In order to transition from amorphous to crystalline particles,[14] and to provoke early nucleations to control the NC size dispersity,[20] ultrasounds may be applied to initiate the nanocrystallization process. Indeed, ultrasounds are known to decrease the free energy necessary for the nucleation to take place thanks to the transient formation of cavitation bubbles with very high local pressure and temperature. The so-called sonocrystallization processes[21,22] strongly favor the dye nucleation, thus enhancing the nucleation frequency J which corresponds to the number of nuclei formed per volume and time units. This gives access to smaller NCs with enhanced crystallinity and lower size dispersity due to a confinement in time of the nucleation step as previously illustrated by La Mer & Dinegar.[23] Indeed, the production of monodisperse NC colloids requires a temporally discrete nucleation step followed by slow growth of nuclei. Nevertheless, upon ageing, the colloids can still evolve due to the Ostwald ripening mechanism through the residual solubility of the dye in solution.[24]

In this context of significant difficulties encountered both in the preparation of molecular NCs and in their structural characterizations, we present in this paper a new versatile sonocrystallization method that couples the injection of an organic solution into water simultaneously with the application of ultrasounds. We have tested and optimized this method with the CMONS dye (α-[(4'-methoxyphenyl)methylene]-4-nitro-benzene-acetonitrile, Figure 1c). Indeed, CMONS is particularly interesting both for its optical properties and for its high complexity through a wealth of polymorphism and associated crystal morphologies. CMONS dye is a stilbene derivative that can present interesting optical power limiting properties[25], intense fluorescence emissions in the crystal state and quadratic nonlinear optical properties (Table S1). Its *trans* diastereomer can be crystallized as three known polymorphs, close in energy and which have all been structurally characterized by single crystal X-ray diffraction.[26,27] As these polymorphs exhibit different optical properties (Table S1), this makes the control of the polymorphism of particular interest. Up to now, CMONS NCs have been embedded in sol-gel thin films, or organosilica-coated NCs, either in their *trans-I* or *trans-III* form.[26,28] Using the proposed sonocrystallization method, we reached a good control on the polymorphism, the *cis*/*trans* isomerization, and the morphology through the nucleation and growth of uniform CMONS needles and nanocubes. The crystallinity of the needles was characterized in depth by powder X-ray diffraction (PXRD), electron diffraction, fluorescence spectroscopy, and solid-state NMR (ssNMR) enhanced by Dynamic Nuclear Polarization (DNP). The mechanism of formation of the needles is also presented.

Experimental section

Methods

CMONS was prepared according to a previously published procedure,[29] and recrystallized twice from toluene. Methanol (HPLC grade) and ultrapure water (HPLC with gradient grade) were purchased from Fisher Scientific. Cetyltrimethylammonium bromide (CTAB) was purchased from Alfa Aesar. Centrifugation was performed with a Beckman Coulter Allegra 64R equipment in 50 mL tubes with a rotation speed of 21 000 rpm, *i.e.* an acceleration of 41 400 *g*. The ultrasounds were produced with a Sonics 500 W generator working at 20 kHz and generating 35 to 500 W (7 to 100% of the nominal power) through a 13 mm tip.

Synthesis

Preparation of pure trans-I CMONS needles (CMONS-N_2). A 1 L beaker with a magnetic stir bar was filled with ultrapure water (600 mL) and placed in a water/ice bath, then N_2 gas was bubbled for 5 minutes into the water. The injection capillary was placed in water under the ultrasonic probe (Figure 1a). A methanol solution of CMONS (100 mL, 2.5×10^{-4} M) was degassed for 2 minutes by bubbling N_2 then introduced into the reservoir. The ultrasounds generator was turned on (7% of the nominal power, 35 W) then the pressure was adjusted to maintain a constant flow (3 mL/min) of CMONS-methanol solution. After all the solution was injected, the ultrasounds were shut off and the pressure was released. During the experiment, the temperature raised from 0 to 15 °C. The CMONS suspension was centrifuged for 30 minutes, then the yellow needles were resuspended in a minimum amount of water using mild ultrasonic radiation, combined and washed twice with water. Finally, the needles were dried *in vacuo* in a tube connected with a P_2O_5-filled Schlenk tube. A dry yellow powder was obtained (6 mg, 85% yield). For the preparation of CMONS-air, no bubbling was performed, while for CMONS-O_2, O_2 was bubbled instead of N_2 gas in the water and CMONS-methanol initial solutions.

Preparation of CMONS nanocubes. A 1 L beaker with a magnetic stir bar placed in a water/ice bath was filled with water (600 mL) and degassed for 5 minutes by bubbling N_2 before adding CTAB (91 mg, 2.5×10^{-4} mol). The injection capillary and the ultrasonic probe were adjusted, and the surfactant was then dissolved under sonication for 5 minutes. The injection of the CMONS-methanol solution was carried out as described above, yielding a stable yellow colloid.

Preparation of trans-I CMONS microcrystals (CMONS-micro).[26] In a 100 mL round-bottom flask, CMONS (0.35 g) was dissolved in hot dichloromethane (15 mL), then the solution was left to concentrate under ambient atmosphere for three days. The solid was composed only of the *trans-I* phase as revealed by PXRD (Fig S1). The morphology was investigated by (FESEM), revealing the presence of large blocks (Fig S2).

Preparation of trans-I CMONS single crystals.[26] CMONS was dissolved in boiling glacial acetic acid. Upon slow cooling, yellow long needles of *trans I* CMONS single crystals were obtained, together with some orange needles. A single yellow needle was selected for single crystal X-Ray analysis.

Characterizations:

Field Emission Scanning Electron Microscopy: FESEM images were recorded using a Zeiss Ultra+ scanning electron microscope. The CMONS NCs in powder were deposited on doped silicon wafers for observation. Alternatively, 3 µL of a dilute colloid were dried on a piece of silicon wafer. A voltage of 3 kV was used at a working distance of 3 mm.

Transmission electron microscopy: TEM was performed on a Philips CM300 microscope operating at 300 kV at 100 K using a sample holder cooled with liquid nitrogen. The TEM grid was prepared by depositing a dilute drop of colloid collected just after synthesis on a carbon-coated copper grid. Images and diffraction patterns were collected on a TemCam F416 TVIPS, which is a rapid, large field of view, high-resolution and high dynamic range CMOS camera (4k×4k, 16 bits). Diffraction patterns were recorded with an exposure time of 0.4 s corresponding to a dose of 0.2 electrons/$Å^2$ to avoid sample damage, while NC images were obtained with 0.4-1s exposure time (dose 0.2 to 0.5 electrons/$Å^2$).

Powder X-ray diffraction: PXRD data of the pure microcrystalline dye and the CMONS needles were collected either on a Bruker D8 Advance diffractometer equipped with a monochromatic Cu Kα1 (λ = 1.5406 Å) source, or on a D8-Endeavor diffractometer with a mixed Kα1 and Kα2 Cu radiation, both operated in a Bragg-Brentano geometry. The data were collected from 2θ, 5 – 50˚ with a 0.01˚ or a 0.02° step size, respectively. A Lynxeye linear detector was used for data collection. The coherent lengths of the crystallites were obtained using the Debye Scherrer formula on single reflections, after determination of the instrumental broadening.

Single crystal XRD: Experiments were carried out using a Nonius Kappa-CCD diffractometer. Cell determination was performed using a ϕ/χ method. The NC size was analyzed in colloidal solutions by dynamic light scattering (NanoKin DLS, Cordouan, France) and the ζ potentials were determined using a Wallis analyzer (Cordouan, France) after dilution in 10^{-3} M NaCl.

Absorption and fluorescence: The spectra were recorded on aqueous suspensions using a SAFAS Xenius XC Cuvette spectrofluorometer with a Xenon source UV lamp. Fluorescence quantum yields were measured using a Horiba-Jobin Yvon Fluorolog-3 spectrofluorimeter equipped with a Hamamatsu R928 photomultiplier tube. The spectra were reference-corrected for both the variation in light intensity of the excitation source and the emission spectral response. Measurements were performed using a calibrated integrative sphere collecting all the emission (2π steradians covered with spectralon), model F-3018 from Horiba Jobin Yvon.

DNP-enhanced ssNMR: The samples were prepared by impregnation of the needles with a DNP matrix composed of 10 mM AsymPolPOK[30] in a d_8-glycerol:D_2O:H_2O (6:3:1) mixture. The amounts of the different CMONS-DNP samples were: 20 mg CMONS-air with 20 μL DNP matrix, 35 mg of CMONS-N_2 with 35 μL DNP matrix, and 40 mg of CMONS-micro with 40 μL DNP matrix. Each impregnated sample was then packed into a 3.2 mm outer-diameter sapphire rotor. All experiments were performed on a Bruker Avance III 400 MHz (^{1}H resonance frequency) DNP-ssNMR spectrometer equipped with a 263 GHz gyrotron for microwave irradiation, a corrugated transmission line and a low temperature 3.2 mm magic-angle sample spinning (MAS) probe used in double-resonance mode.[31] All experiments were performed at a sample temperature of 100 K, and a MAS frequency of 12.5 kHz for ^{13}C- and 8 kHz for ^{15}N spectra, unless stated otherwise.

Cross-polarization under MAS[32] (CPMAS) experiments were performed with a radio frequency (rf) field strength of 50 kHz on ^{13}C /^{15}N and 100 kHz on the ^{1}H channel. A 50-to-100% ramp was used for the ^{1}H CP spin-lock during CP.[33–36] The CP contact time was set to 2 ms after optimization. ^{1}H decoupling at a field strength of 100 kHz using SPINAL-64[37] was applied during acquisition. The inter-scan delay was optimized according to the polarization build-up time of each sample, and set to 9.75 s for CMONS-micro, 6.0 s for CMONS-air, and 6.5 s for CMONS- N_2. 64 transients were accumulated for each ^{1}H-^{13}C CPMAS experiment while 256, 512, and 2048 transients were added for the ^{1}H-^{15}N CPMAS experiment on CMONS-N_2, CMONS-micro, and CMONS-air, respectively.

Results and discussion

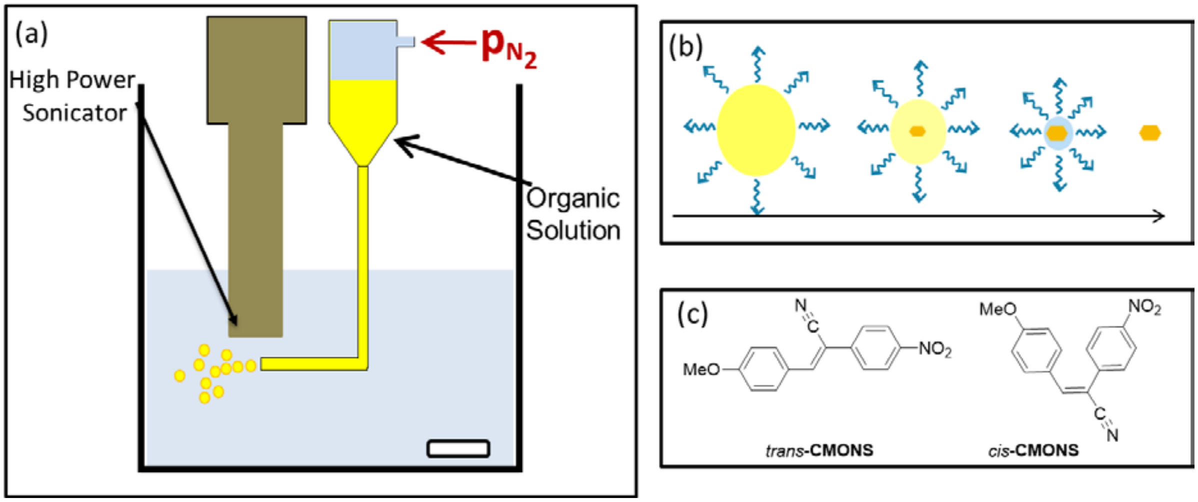

Figure 1: (a) Scheme of the setup developed for the nanocrystallization of organic compounds; (b) Principle of the nucleation and growth of a single NC from an initial droplet of organic solution gradually mixed with water. (c) trans and cis diastereomers of CMONS.

We designed an original sonocrystallization reactor (Figure 1a) to prepare aqueous colloidal solutions of organic NCs. The process is based on the injection into ultrapure water of a solution of the organic compound dissolved in a water-miscible organic solvent. The reservoir containing the organic solution is connected to a capillary (*ca* 20 cm long and 0.17 mm in diameter) allowing the injection of a constant flow of organic solution into water. The control of the solution flow is achieved by applying a constant nitrogen pressure to the tank, in the 0.5-2 bar range. The end of the capillary, corresponding to the injection area of the organic solution, is immersed in water, around 5 mm below an ultrasonic probe which delivers a constant power. It can be easily checked by direct visualization that ultrasounds fragment the flow of organic dye solution into micron-sized droplets (Figure 1b). Then, by progressively mixing the organic solvent containing the dye with water, the volume of droplets is gradually reduced, thus increasing the dye saturation in droplets. Finally, at high supersaturation, the dye nucleation and growth take place under confined conditions in space (Figure 1b). As the nucleation step occurs at the end of solvent dispersion in water within micron-sized droplets, only a single nucleus should be formed in each droplet as a result of the confined conditions of nucleation.[38] Indeed, the probability dP of forming a stable nucleus in a volume of solution V during a period of time dt is dP = J V dt, where J is the stationary nucleation rate, or nucleation frequency. The other effect of the ultrasonic radiation is to provoke the formation of cavitation bubbles, which can promote the nucleation process either in the bubbles, associated with very high local pressure, or at their interface with the solution through heteronucleation.[20]

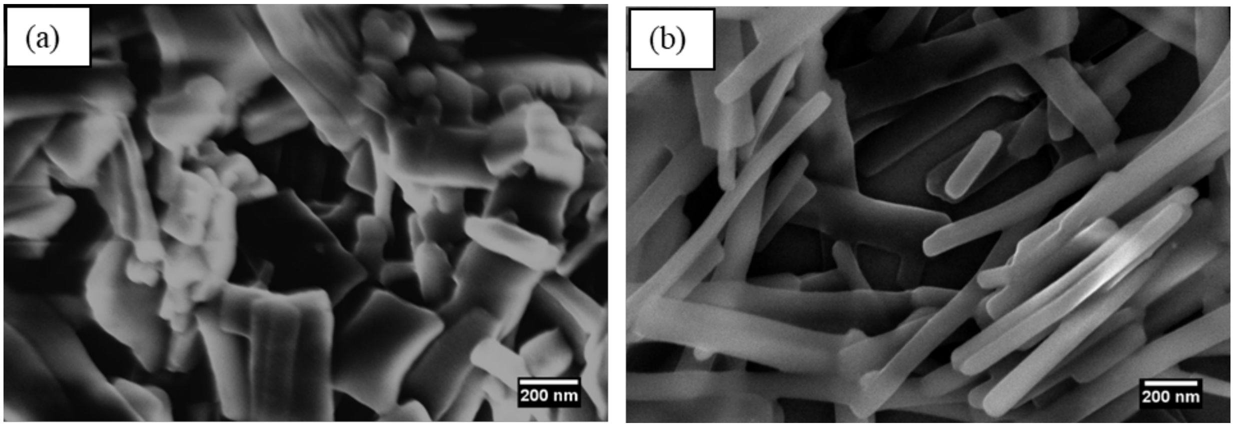

Figure 2: SEM of the CMONS-N_2 needles (a) without or (b) with 35 W of applied ultrasounds.

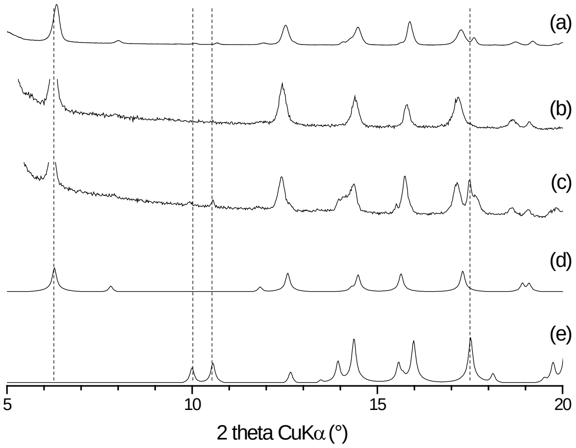

Figure 3: PXRD of the obtained yellow needles obtained under varied conditions: (a) CMONS-air; (b) CMONS-N_2; (c) CMONS-O_2; (d) reference *trans-I* CMONS;[27] (e) Reference *cis*

CMONS.[27] Dashed lines highlight selected peaks from the *cis* isomer.

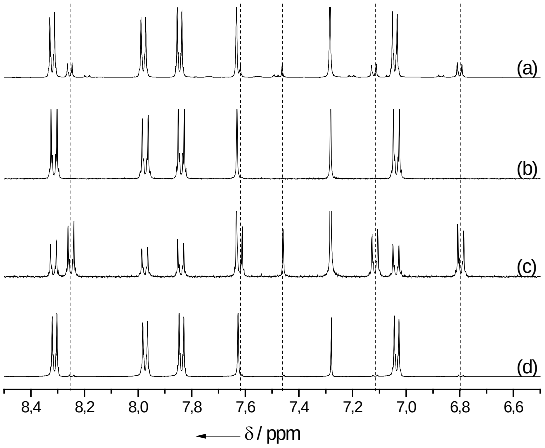

Figure 4: Solution-state ^{1}H NMR in $CDCl_3$ of (a) CMONS-air; (b) CMONS-N_2; (c) CMONS-O_2; (d) starting CMONS. Dashed lines highlight selected signals from the *cis* isomer.

To estimate appropriate concentrations for the synthesis of NCs, an approximate calculation shows that a spherical droplet with a diameter of 5 µm of an organic solution at 2.5×10^{-4} M should lead to a 0.15 µm wide nanocube. Thus, the first trials of sonocrystallization were intended by injecting 100 mL of a methanol solution of CMONS at a concentration of 2.5×10^{-4} M into 600 mL of water under standard precipitation conditions. DLS of the obtained yellow fluorescent suspension evidenced the formation of micron-sized objects instead of the expected NCs, while SEM micrographs revealed the presence of submicron needles, yet polydisperse in width and length (Figure 2a). Satisfactorily, upon applying a moderate power of ultrasounds (35 W), uniform needles, 1-2 µm long with a diameter of 82 ± 17 nm (CMONS-air, Figure S3) were observed by SEM. This ultrasound effect was investigated: starting from a power of 35 W, an increase of the power to 150 W yielded similar results in terms of size and crystallinity. Furthermore, the solvent nature, the concentration of the organic solution, and the water/CMONS solution ratio were varied, but had little effect on the dimensions of the obtained needles. The monodispersity observed under sonication (Figure 2b) clearly illustrates the interest of our sonocrystallization method to generate a confinement of the CMONS crystallization in micrometer size droplets. The presence of sharp PXRD peaks suggests high crystallinity (Figure 3a). A close look at the diffractogram reveals that the powder is mainly composed of the *trans-I* form of CMONS, in agreement with the intense yellow fluorescence emission of the powder.[26] Surprisingly, a small fraction of the *cis* form of CMONS is also visible by PXRD, even if the CMONS starting powder only shows the presence of the *trans* isomer (Figure 1c). A more quantitative information was obtained by NMR in solution after dissolving the starting powder and the obtained needles of CMONS-air in $CDCl_3$ (Figure 4). Though the starting CMONS only featured 2.5% of the *cis* form, this *cis* fraction increased to 20% after sonocrystallization. *Trans-cis* isomerization of double bonds at room temperature is rather unusual. We believe it may be due to the high power ultrasounds applied in this process, which are known to form oxygen radicals HO° and/or HOO° from dissolved dioxygen.[39] To check this hypothesis, we compared PXRD (Figure 3) and solution-state NMR (Figure 4) characterizations of the CMONS-air sample with those obtained under similar conditions, but after bubbling either oxygen (CMONS-O_2) or nitrogen (CMONS-N_2) in the CMONS-methanol and ultrapure water initial solutions. Both PXRD and solution-state NMR experiments confirmed the absence of the *cis* form in CMONS-N_2. Conversely, the *cis* isomer was dominating when oxygen was bubbled instead of nitrogen (60% *cis* in CMONS-O_2). This is a clear indication that oxygen radicals are formed from dissolved dioxygen under sonication, and are implied in the isomerization process of CMONS molecules.[40] A mechanism for this *trans*-to-*cis* isomerization is proposed in Figure S4. It is noteworthy that the *cis* isomer is not visible at all by solution-state NMR after sonocrystallization with N_2 bubbling (Figure 4b) while the starting CMONS contained 2.5% of this form. Therefore, it is possible to obtain needles of the pure *trans-I* form for CMONS-N_2 with dimensions of 98 ± 33 nm width and *ca* 2 µm length if a careful N_2 bubbling in the initial solutions is applied (Figure 2b).

The crystal quality of CMONS-N_2 needles was first probed locally by electron diffraction in a transmission electron microscope. Indeed, this technique allows to determine the crystallinity and the structural arrangement at the nanoscale. However, CMONS-N_2, similarly to other organic samples, is particularly fragile under the electron beam. The analysis was therefore performed under low dose using a voltage of 300 kV, and at low temperature (100 K) following the techniques developed for silica-coated organic NPs in our laboratory.[28,41] Despite the presence of bundles of needles on the grid as previously observed in SEM images, it was possible to obtain a diffraction pattern from a single needle, as seen in the TEM image (Figure 5a). Fortunately, as the needles feature a parallelepipedal form, the observed needle was lying on the $(\vec{a}, \vec{b})$ face, which led to the [001] electron diffraction pattern. Cell parameters $a^* = 0.26$ Å^{-1} and $b^* = 0.08$ Å^{-1} identical to the ones calculated from the reciprocal cell parameters of the *trans-I* form could be measured, and the diffraction pattern was indexed (Figure 5b). The presence of a single set of spots indicates that the observed zone (*ca* 500 nm in diameter, yellow circle in Figure 5) is monocrystalline. However, some reflections forbidden in the $P2_1/n$ (14) space group are visible, and may be attributed to structural modifications occurring under the electron beam: the quite intense reflections $0k0$ with $k = 2n+1$ can be explained by a loss of symmetry of the structure (helicoidal axis 2_1 // b disappearance in this case). The reflections $h0l$ with $h+l = 2n+l$ are weakly re-ignited, probably due to multiple diffraction, but perhaps also due to the loss under irradiation of the glide plane n perpendicular to the b axis. The irradiation may have induced atomic displacements[42] in CMONS molecules, prior to the final amorphization of the material under the electron beam.

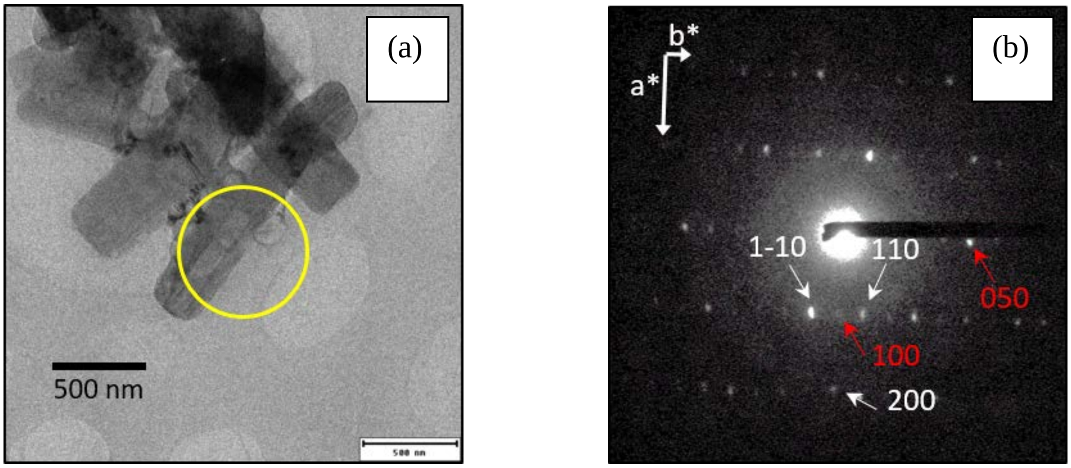

Figure 5: (a) TEM micrograph of CMONS-N_2 needles and (b) [001] electron diffraction pattern of the selected zone (yellow circle on the micrograph). Forbidden reflections due to multiple diffraction and/or lack of symmetry are indexed in red.

This TEM and electron diffraction measurements enabled to determine that the main axis of the needle lies in the (*a**, *b**) plane. To unambiguously assign the direction of preferential growth, we grew single crystals (2000 × 60 × 60 µm) of *trans-I* CMONS from acetic acid (Figure S5) and studied them by single crystal X-Ray diffraction analysis. Following the determination of the cell and the orientation matrix (using evalCCD14, from Nonius Package), the crystal was oriented perpendicular to the *c*-axis as displayed in Figure S5. This showed that the main axis of the needles is indeed the *a*-axis, corresponding to a preferential growth by π-π stacking.

The crystallinity of the CMONS needles obtained by sonocrystallization was then probed by monochromatic PXRD studies (Figure S1) in the case of CMONS-air, CMONS-N_2 and CMONS-micro. For all samples, the PXRD analysis could not detect any visible amorphous parts, as no bump was observed on the very weak background at low diffraction angles. A Le Bail refinement at 298 K was performed for all three samples. The space group and cell parameters for CMONS-

N_2 and CMONS-micro were in good agreement with the published parameters for the *trans-I* form (Table 1), and very different from the two other known polymorphs of *trans* CMONS.[27] The slight variations between the two sets of cell parameters of the *trans-I* form may arise from temperature differences between the present (298 K) and published (123 K) measurements. For CMONS-air, a major set of reflections could be assigned to the *trans-I* form of the CMONS, while the minor set of reflections could be unambiguously assigned to the *cis* form (Table 1 and S1), in agreement with the solution-state NMR results. The analysis of the width of the (004) and (022) reflections gave similar coherence lengths, corresponding to single crystal domains, in the (b, c) plane for the *trans-I* form for CMONS-N_2 and CMONS-air (Table 1). The values are very close to the width of the needles (80-100 nm) evidencing a high crystal quality for the needles. The largest coherence length was found for CMONS-micro, but this value appears however low for a microcrystalline sample. Indeed, the SEM micrographs (Figure S2) show that CMONS-micro is constituted of assembled needles and blocks of sub-micron sizes.

However, no usable coherence length along the main axis of the needle could be obtained due to the small value of the *a*-parameter, which leads to reflections appearing in the region over 25° where no individual peaks could be isolated.

	Space group	a (Å)	b (Å)	c (Å)	β (°)	Coherence length (nm) [a]	Coherence length (nm)[b]
CMONS-N_2	$P2_1/n$	3.8891(5)	12.347(1)	28.787(5)	93.16(1)	46 ± 5	54 ± 5
CMONS-micro	$P2_1/n$	3.8918(3)	12.366(2)	28.669(5)	92.82(2)	65 ± 5	62 ± 5
CMONS-air (*major*)	$P2_1/n$	3.8766(6)	12.316(2)	28.689(5)	93.136(4)	53 ± 5	51 ± 5
CMONS-air (*minor*)	$P2_1/c$	8.692(2)	12.679(2)	12.523(2)	101.74(1)	-	-
Reference *trans-I* [c]	$P2_1/n$	3.814(1)	12.371(3)	28.132(5)	91.50 (2)		
Reference *cis* [c]	$P2_1/c$	8.543(3)	12.697(4)	12.572(4)	101.52 (3)		

Table 1: Results of the Le Bail refinement of the three CMONS samples (see Fig S1). [a] Determined for the (004) reflection; [b] Determined for the (022) reflection. [c] From the crystal structures in ref [27], determined at 123 K.

Besides X-ray and electron diffraction techniques CMONS NCs were further investigated using DNP-enhanced ssNMR.[43,44] This hyperpolarization technique relies on the use of paramagnetic dopants, also called polarizing agents (PAs), which are added to the studied material. Under microwave irradiation, the large electron spin polarization of the PAs is transferred to the surrounding nuclear spins, allowing the detection of a much stronger NMR signal. For proton-dense materials, the transfer of polarization from electron to ^{1}H nuclear spins is particularly efficient for nano-sized particles,[45] leading to unprecedented sensitivity and experimental time saving, and thus enabling in-depth atomic scale characterization of materials at natural isotopic abundance (1.1% for ^{13}C and 0.37 % for ^{15}N).[46–54]

In a first step, we checked that the experimental DNP specific conditions (impregnation with a glycerol and PA containing solution, sample temperature of 100 K) did not affect the CMONS needles. As shown in Figure 6, the ^{13}C resonances of CMONS-N_2 under DNP conditions (Figure 6b) are very similar to the ones of CMONS-micro observed at room temperature with standard ssNMR (Figure 6a). In each case, the relatively narrow ^{13}C/^{15}N linewidths are consistent with a crystalline material. Nevertheless, it is interesting to note that despite the low sample temperature and the presence of paramagnetic dopants, the ^{13}C resonance linewidth of CMONS-N_2 needles is slightly smaller than the one of CMONS-micro (80-85 Hz full-width at half-height vs. 100-105 Hz). This might indicate less defects and/or local disorder compared to the larger CMONS microcrystals, however a change in Anisotropic Bulk Magnetic Susceptibility (ABMS) cannot be ruled out.[55–58] Indeed ABMS broadening have reportedly been observed in organic solids containing phenyl groups.[57,58] In comparison, the resonances in the DNP-enhanced ssNMR spectrum of CMONS-air (Figure 6c) are slightly broader than in the CMONS-N_2 case, and additional small peaks (indicated by a hash) are detected, due to the presence of the minor *cis* diastereomer. The resonances in CMONS-air are broadened by the overlapping of *trans* and *cis* resonances arising from a NC mixture of *trans-I* and *cis* forms as previously evidenced by PXRD (Figure 3).

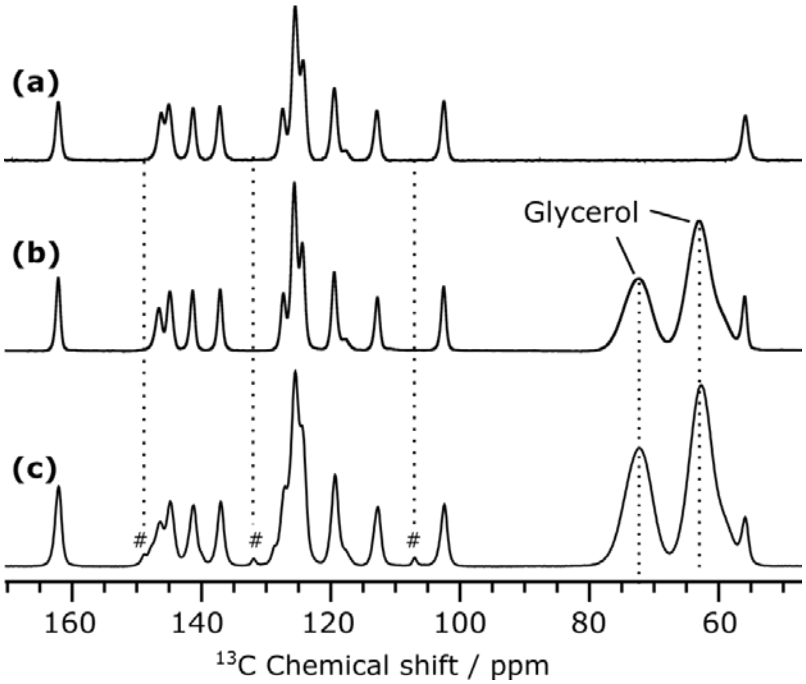

Figure 6: (a) ^{1}H-^{13}C-CPMAS ssNMR spectrum of pure CMONS-micro powder at room temperature. (b)-(c) ^{1}H-^{13}C-CPMAS DNP-enhanced ssNMR spectra of CMONS-N_2 (b) and CMONS-air (c) at 100 K. Glycerol peaks resulting from the impregnation with the DNP matrix in (b) and (c) are indicated. Resolved peaks of the *cis* diastereomer visible in (c) are labeled with a hash, and their position is marked through all three spectra with vertical dotted lines.

The signal enhancement provided by DNP is highlighted in Figure 7, which compares spectra acquired with and without microwave (μw) irradiation. The gain in signal intensity is important for all samples, ranging from a factor 8 for CMONS-micro to 19 and 35 for COMNS-air and CMONS-N_2, respectively. The variation in DNP enhancement factor going from micro-sized to nano-sized particles can be rationalized easily. As the polarizing agent molecules cannot penetrate inside the crystal particles, the ^{1}H hyperpolarization needs to propagate through the particles with ^{1}H-^{1}H spin diffusion, which results in higher sensitivity improvement for smaller objects.[45] The variation in DNP enhancement factors between CMONS-air and CMONS-N_2 needles could be due to a change in aggregation state, which could influence the wetting of the nanocrystals with the DNP matrix.

It is also worth noting that the ^{13}C linewidth does not change when applying the microwave irradiation in the case of CMONS-N_2 (Figure 7 b) and CMONS-air (Figure 7 c), while this is not the case for CMONS-micro (Figure 7 a). This effect might be interpreted as follows: the CMONS needles are uniformly polarized such that the same linewidth with and without microwaves is observed, whereas we can expect that the CMONS microcrystals are non-uniformly polarized, favoring the possibly less crystalline outer shell (hundreds of nm) of the microcrystals in the DNP-enhanced spectrum, resulting in broader lines compared to the spectrum without microwaves. This observation confirms the excellent crystallinity of the CMONS needles.

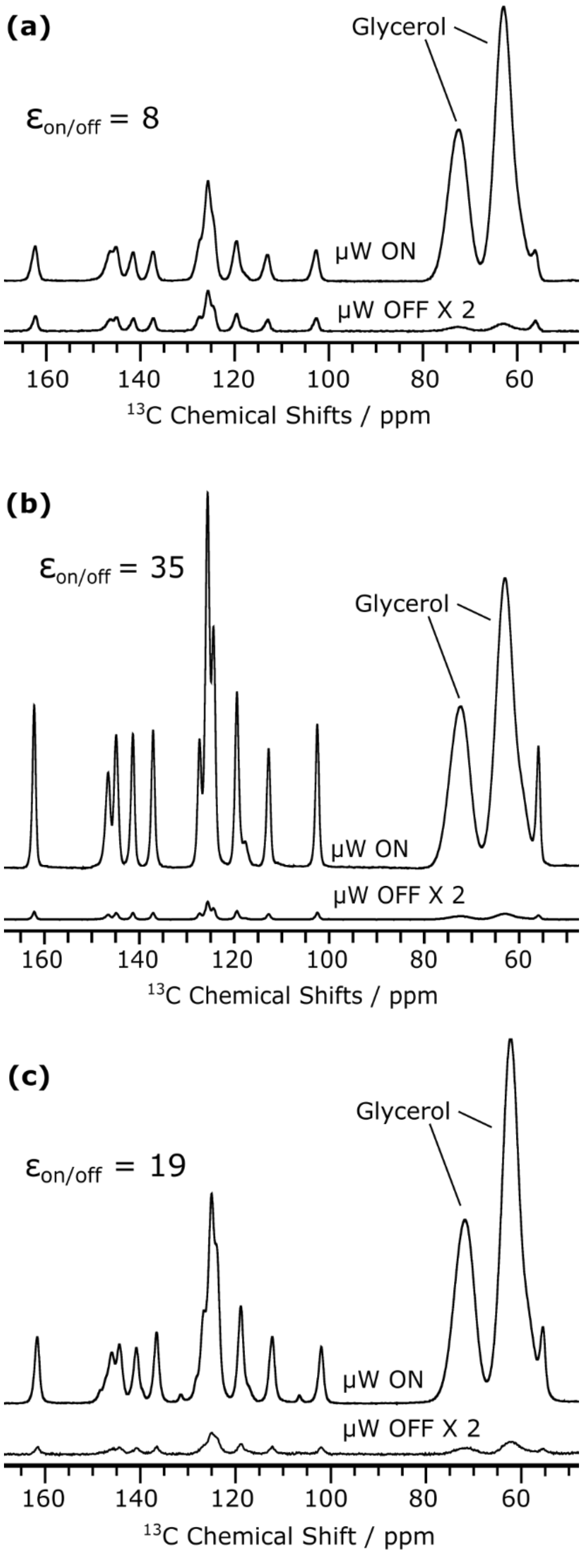
(a)
$\varepsilon_{on/off}$ = 8
Glycerol
μW ON
μW OFF X 2
160
140
120
100
80
60
^{13}C Chemical Shifts / ppm
(b)
$\varepsilon_{on/off}$ = 35
Glycerol
μW ON
μW OFF X 2
160
140
120
100
80
60
^{13}C Chemical Shifts / ppm
(c)
$\varepsilon_{on/off}$ = 19
Glycerol
μW ON
μW OFF X 2
160
140
120
100
80
60
^{13}C Chemical Shift / ppm

Figure 7: ^{1}H-^{13}C -CPMAS DNP-enhanced ssNMR spectra (μw on, top spectra) of (a) CMONS-micro, (b) CMONS- N_2, and (c) CMONS-air, compared to the spectra (intensity scaled by a factor × 2) acquired without μw irradiation (μw off, bottom spectra). Values of $\varepsilon_{\mathrm{on/off}}$, the signal intensity ratio between experiments performed with and without microwave irradiation, are given in each panel for the CMONS signals. For the glycerol signals, $\varepsilon_{\mathrm{on/off}}$ is 74, 82, and 67 for (a), (b), and (c), respectively.

To complement the ^{13}C NMR results, we also used DNP to record natural abundance ^{15}N DNP-enhanced ssNMR spectra of CMONS-micro, CMONS-N_2, and CMONS-air (Figure 8), since it is known that ^{15}N chemical shifts are very sensitive to their local environment. The observations derived from Figure 6 based on ^{13}C NMR chemical shifts are confirmed by the ^{15}N NMR data presented in Figure 8. The narrow linewidth observed in all three spectra underlines again the high crystallinity of the samples. The ^{15}N resonance linewidth of the CMONS-N_2 needles (Figure 8b) is here ~30% narrower than those of the microcrystals (CMONS-micro, Figure 8a), both under DNP conditions. This again can be the result of differences in crystallinity of the hyperpolarized region of the sample (surface layers in case of CMONS-micro *vs*. entire needle for CMONS-N_2) and/or differences in some ABMS broadening.[55–58] The two resonances of the *cis* diastereomer, marked with a hash in Figure 8, are only visible in the CMONS-air sample (Figure 8c). Interestingly, one can note that the cyano ^{15}N resonance is strongly shifted between the *trans-I* and the *cis* form (at respectively 270 and 256 ppm). As expected, the ^{15}N nitro resonance is less affected by the change in molecular configuration (370 ppm for the *trans-I*, and 368 ppm for the *cis*-configuration).

The three ^{15}N DNP spectra shown in Figure 8 correspond to about 5.5 hours of experimental time in total and show excellent sensitivity, required for the detection of multiple polymorphs or amorphous contribution. It is also worth pointing out that such experiments can be proven challenging to record with conventional ssNMR. For instance, it would have taken about 80 days with conventional ssNMR to obtain the three spectra shown in Figure 8 with the same signal to noise.

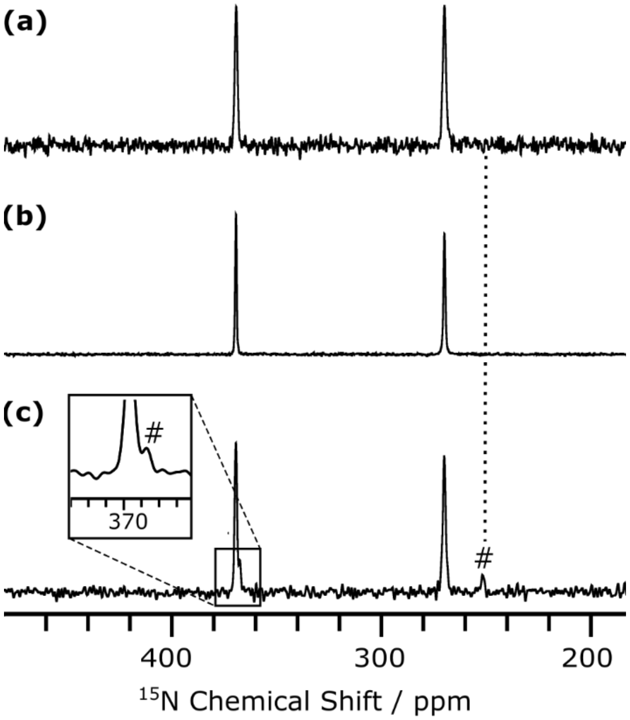

Figure 8: ^{1}H-^{15}N CPMAS DNP-enhanced ssNMR spectra of (a) CMONS-micro, (b) CMONS-N_2, and (c) CMONS-air. The signals of the *cis* diastereomer visible in (c) at 368 and 256 ppm are labeled with a hash. The position of the 256-ppm signal is marked through all three spectra with a vertical dotted line.

On the other hand, we have shown in a previous study that fluorescence spectroscopy can also indirectly not only characterize the nature of the CMONS polymorph obtained during solution crystallization, but also give a good indication on the degree of crystallinity of the crystallites obtained.[26,28] Indeed, the three polymorphs of *trans* CMONS exhibit very different fluorescence emission bands (Table S1).[27,28] Furthermore, the quantum yield (QY) of CMONS dissolved in solution is very low (QY < 1%), while the *trans-I* form has the highest fluorescence emission with a maximum QY of 48% for micron-size powders (CMONS-micro).[59] All suspensions prepared through optimized conditions of sonocrystallization show an intense yellow color and a high fluorescence intensity. The intense fluorescence with a broad emission band peaking at 548 nm (Figure 9) can be attributed to the CMONS *trans-I* polymorph as described previously.[26] On the other hand, the very high fluorescence efficiency with QY up to 38 ± 4 % suggests a high crystallinity of the CMONS-N_2 needles as specified from PXRD and DNP-enhanced ssNMR. Indeed, for this kind of crystal-state fluorophores, any slight distortion leads to fluorescence quenching, thus to a strong decrease in QY. The slight QY decrease observed for CMONS-N_2 compared to the microcrystalline sample is certainly due to surface effects, which become important for these 100 nm thick needles.

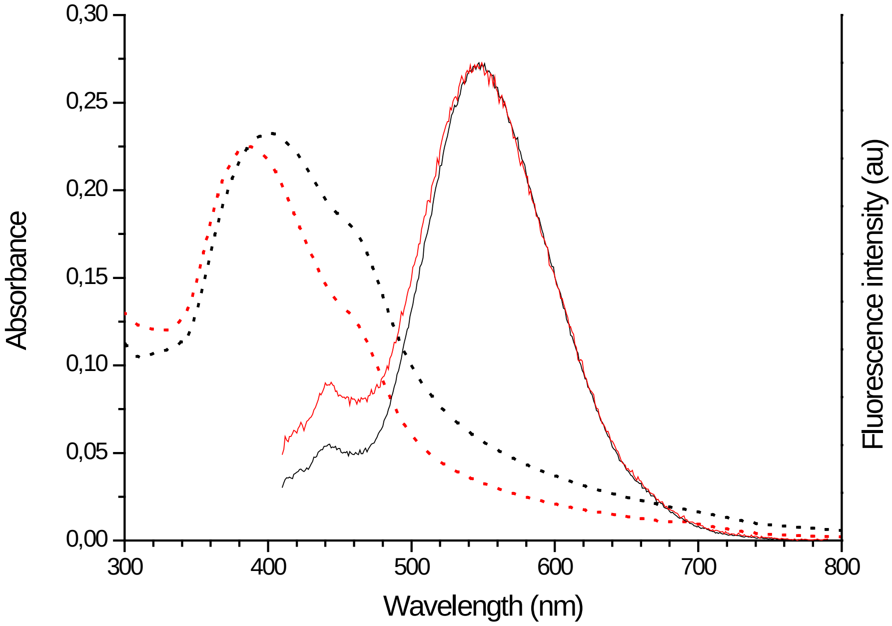

Figure 9: Absorption (dotted lines) and normalized emission spectra (full lines) of CMONS-N_2 needles (in black) and CMONS nanocubes (in red), with λ_{exc} = 400 nm.

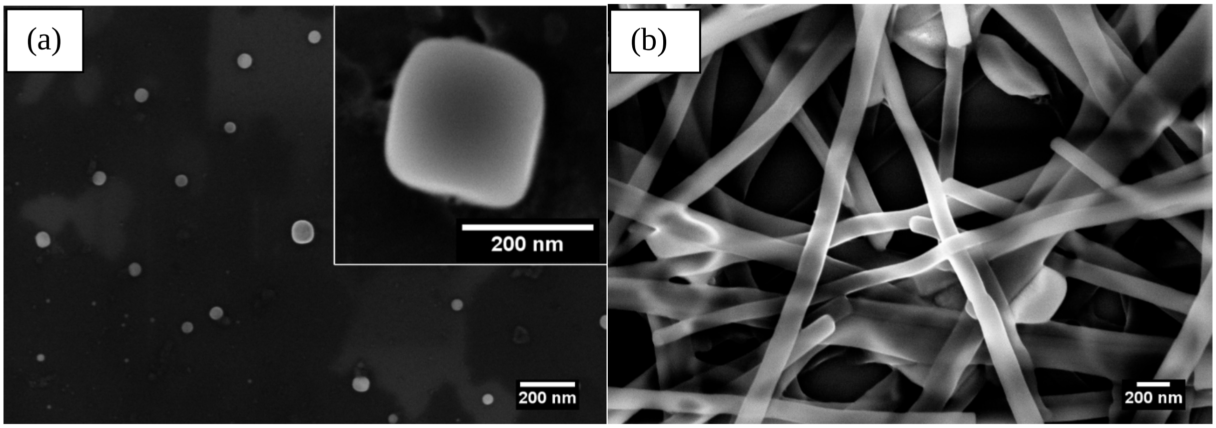

Figure 10: SEM micrographs of (a) CMONS nanocubes obtained in the presence of CTAB, and (b) CMONS needles obtained after dialysis.

Considering the proposed crystallization process, the formation of micron-long needles upon fragmentation of the CMONS-methanol solution stream by ultrasounds is, at first glance, rather intriguing. These needles probably arise from a fast Ostwald ripening of initially formed NCs (primary particles), as firstly hypothesized. In order to confirm this hypothesis on the Ostwald ripening, which is certainly favored by a residual solubility of CMONS (polar molecule) in the final solvent mixture (water + injected methanol), we decided to investigate the effect of additives on the crystallization process. To this aim, various surfactants such as PVP, Brij, Pluronics and CTAB were tried, but only the latter one lead to stable colloids. Indeed, when 10 equivalents of CTAB with respect to CMONS were dissolved in the aqueous phase before injection, stable colloids with DLS size around 400 nm were obtained. SEM on a dried droplet (Figure 10a) evidences the presence of cubes of 100-300 nm in width, consistent with the DLS size. The similarity with CMONS-N_2 in the optical absorption and fluorescence spectra (Figure 9), together with the elevated QY value (21 ± 2% for CMONS nanocubes *vs* 48% for CMONS-micro) and the cubic morphology of the particles suggest the presence of crystals of the *trans-I* form. Accordingly, the NCs are stabilized by CTA^+ cations, as a strongly positive ζ potential of +29 ± 5 mV was measured. When the CTAB was then removed by dialysis against the same water: methanol 6:1 solvent mixture, a precipitate formed, which was identified as 100 nm-thick, 3-5 µm long needles (Figure 10b) similar to those previously observed in CMONS-N_2. Concomitantly, the ζ potential evolved from +29 ± 5 mV to 0 ± 5 mV, in agreement with the removal by dialysis of adsorbed CTA^+ cations from the surface of the CMONS NCs. From these observations, we propose the mechanism presented in Figure 11. Crystalline nanocubes are first formed by confined crystallization within micron-sized droplets obtained by ultrasonic fragmentation of the injected methanol stream, Figure 1. These nanocubes can be stabilized and observed if CTAB is added. However, in the absence of stabilizing agent, typical Ostwald ripening quickly takes place through the residual CMONS solubility in the solution, favoring the growth of needles through strong π-π stacking interactions. In addition, this Ostwald ripening may be coupled to a self-organized aggregation and coalescence mechanism of primary nanoparticles, as it has been previously reported for many other colloidal systems.[60–62] In our case, this ordered aggregation would be favored by the high symmetry of the morphology of the cubic primary particles of CMONS. Indeed, due to the initial nanocubes formation, aggregated primary particles can exhibit very low degree of crystallographic misorientation associated with small surface energy, which yields facile coalescence.[63] Thus, adjoining nanocubes can fuse to form larger crystals leading to the formation of needles. Indeed, the directional selectivity of the coalescence mechanism greatly reduces the interfacial energy of the small primary particles.

On the other hand, it is noteworthy that the *trans-I* form is not the thermodynamically most stable form of CMONS.[26] This confirms that this sonocrystallization process, involving an instant confined nucleation and growth of NCs, is entirely kinetically controlled, allowing thus nanocrystallization of a pure single polymorph. The purity of CMONS-N_2 is also an interesting factor, as it is purely *trans* as evidenced by ^{1}H solution NMR, although the starting CMONS contains 2.5% of the *cis* diastereomer (Figures 3b and 3d). This suggests that the *cis* form remains solubilized at the end of the process. When more *cis* isomer is produced, as it is the case when the water is not degassed of oxygen, the soluble *cis* species start independently to nucleate and grow in solution forming a second crystalline phase, as evidenced by DNP-enhanced ssNMR and PXRD.

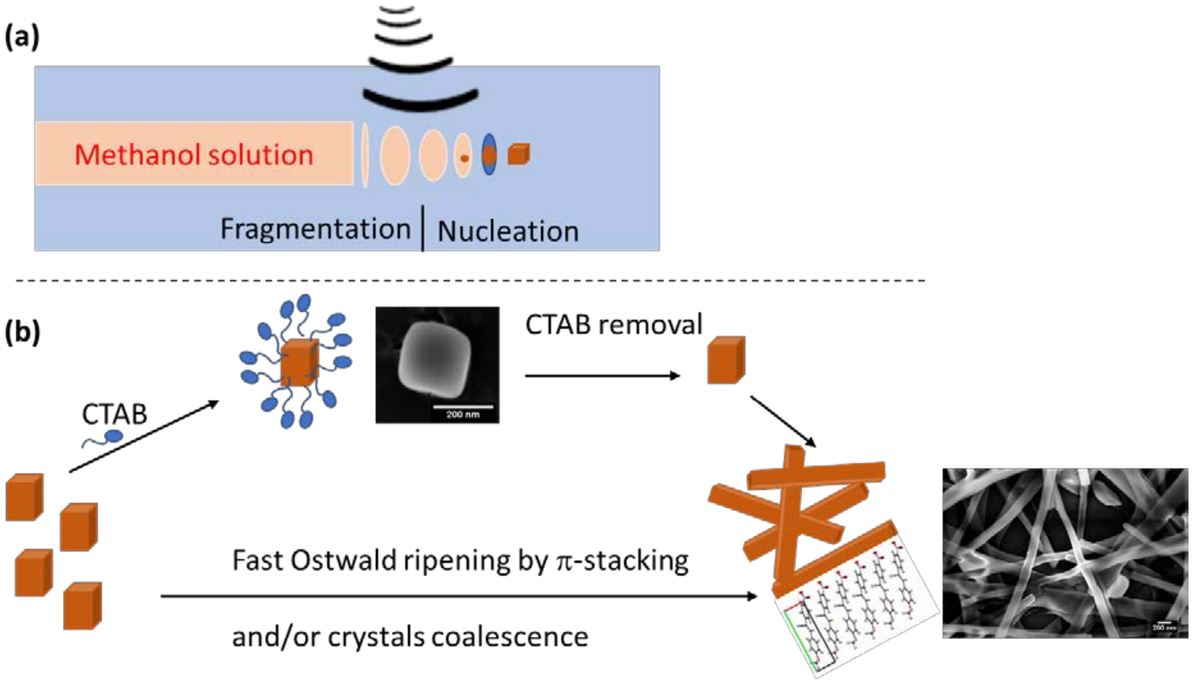

Figure 11: Proposed mechanism for the formation of CMONS needles by sonocrystallization: in the first step, (a) the ultrasounds fragment the CMONS-methanol solution stream into droplets. Each droplet undergoes confined ultrasound-assisted nucleation and growth of a NC. (b)

nanocubes can be stabilized by CTAB or, in the absence of surfactant, they rapidly undergo Ostwald ripening and /or NC coalescence to form needles.

Conclusions

This study shows that confined ultrasound-assisted crystallization can be a useful tool to produce NCs with high crystallinity. In particular, *trans-I* CMONS needles or nanocubes could be obtained with a narrow size distribution and as a single polymorph under kinetic control. This is particularly spectacular for this molecule which easily crystallizes as mixtures of three polymorphs. However, we have found that dissolved dioxygen must be carefully removed from the initial solution when ultrasounds are used, as it causes isomerization of activated double bonds through the formation of transient oxygen radicals. Various tools were used in order to obtain an in-depth characterization of the crystallinity. Electron diffraction at low temperature in a transmission electron microscope enabled to visualize the reciprocal space in a CMONS-N_2 needle, to evidence locally the crystallinity and compare reciprocal distances with those found in the literature. Next, single crystal X-ray diffraction allowed to unambiguously attribute the acicular axis of the needle to the *a* crystallographic axis, which logically corresponds to a packing by π-π stacking. The classical PXRD technique provided statistical information enabling the refinement of the crystal cell parameters, not only in the case of a pure polymorph, but also for the 4:1 *trans I*: *cis* mixture obtained for CMONS-air. The coherence lengths (~50 nm) deduced for CMONS-N_2, corresponding to half the width of the needles, reflect the average length for which the repetitions are geometrically defect-free. To obtain information about the chemical environment around each carbon and nitrogen atoms, ^{13}C and ^{15}N DNP-enhanced ssNMR spectra of the samples were recorded. This technique, particularly efficient for nano-crystalline samples, enabled the acquisition of ssNMR spectra with enhancement factors up to 35 for CMONS-N_2. This permitted to get in few minutes, respectively few hours, high quality ^{13}C and ^{15}N 1D spectra at natural abundance with only 20-40 mg of sample. In all cases, narrow signals were observed, confirming the high crystallinity of the samples. The presence of the minor *cis* diastereomer in CMONS-air could be detected both in ^{13}C and ^{15}N spectra through the presence of additional resolved peaks. The high sensitivity obtained by DNP-enhanced ssNMR on such nano-sized crystalline materials is very promising for further structural investigation of the molecular packing, which is however out of the scope of this study.

Altogether these techniques unambiguously evidence the high crystal quality of the sono-crystallized needles. Additionally, both PXRD and DNP-ssNMR enable to evidence that the different samples are exempt of amorphous parts, and that CMONS-air is composed of two distinct crystallographic phases without cocrystals of *cis* and *trans I* isomers. However, a more precise evaluation of the relative crystallinity of the different samples is precluded by experimental limitations, such as ABMS for DNP-ssNMR or surface quenching for fluorescence spectroscopy.

Finally, the mechanism of the formation of CMONS needles was ascertained after addition of the CTAB surfactant, which stabilizes transient *trans-I* CMONS nanocubes towards Ostwald ripening. This typical growth process by Ostwald ripening could be associated to a self-organized aggregation and coalescence mechanisms of primary nanoparticles favored by their high cubic symmetry. Further evidence on the generalization of this ultrasound-assisted reprecipitation method to obtain colloids of small fluorescent organic NCs will be reported soon.

Supporting Information. Monochromatic XRD patterns of CMONS-air, CMONS-N_2 and CMONS-micro; SEM of CMONS-micro, CMONS-air and CMONS-N_2; Mechanism of *trans*-to-

cis isomerization, photograph of oriented CMONS *trans I* single crystal and associated structure; properties of the different CMONS polymorphs.

Author Contributions

The manuscript was written through contributions of all authors. All authors have given approval to the final version of the manuscript.

ACKNOWLEDGMENT

Christophe Bouchard is gratefully acknowledged for helping realizing the nanocrystallization setup. Yann Bretonnière (ENS Lyon) is gratefully acknowledged for performing QY measurements. This work was supported in part by the French National Research Agency (CBH-EUR-GS and Labex ARCANE ANR-17-EURE-0003, Glyco@Alps ANR-15-IDEX-02, and ANR-16-CE11-0030-03). Part of this work, carried out on the Platform for Nanocharacterisation (PFNC), was supported by the "Recherche Technologique de Base" program of the French National Research Agency (ANR).

REFERENCES

(1) Baba, K. Functional Organic Nanocrystals; Kasai, H., Ed.; IntechOpen: Rijeka, 2011; p Ch. 15. https://doi.org/10.5772/16948.

(2) Kasai, H.; Nalwa, H. S.; Oikawa, H.; Okada, S.; Matsuda, H.; Minami, N.; Kakuta, A.; Ono, K.; Mukoh, A.; Nakanishi, H. A Novel Preparation Method of Organic Microcrystals. *Jpn. J. Appl. Phys.* **1992**, *31* (Part 2, No. 8A), L1132–L1134. https://doi.org/10.1143/jjap.31.l1132.

(3) Nalwa, H. S.; Kakuta, A.; Mukoh, A.; Kasai, H.; Okada, S.; Oikawa, H.; Nakanishi, H.; Matsuda, H. Fabrication of Organic Nanocrystals for Electronics and Photonics. *Adv. Mater.* **1993**, *5* (10), 758–760. https://doi.org/https://doi.org/10.1002/adma.19930051018.

(4) Ibanez, A.; Maximov, S.; Guiu, A.; Chaillout, C.; Baldeck, P. L. Controlled Nanocrystallization of Organic Molecules in Sol-Gel Glasses. *Adv. Mater.* **1998**, *10* (18), 1540–1543. https://doi.org/10.1002/(SICI)1521-4095(199812)10:18<1540::AID-ADMA1540>3.0.CO;2-1.

(5) Yang, X.; Ong, T. C.; Michaelis, V. K.; Heng, S.; Huang, J.; Griffin, R. G.; Myerson, A. S. Formation of Organic Molecular Nanocrystals under Rigid Confinement with Analysis by Solid State NMR. *CrystEngComm* **2014**, *16* (39), 9345–9352. https://doi.org/10.1039/C4CE01087F.

(6) Schilt, Y.; Berman, T.; Wei, X.; Barenholz, Y.; Raviv, U. Using Solution X-Ray Scattering to Determine the High-Resolution Structure and Morphology of PEGylated Liposomal Doxorubicin Nanodrugs. *Biochim. Biophys. Acta - Gen. Subj.* **2016**, *1860* (1, Part A), 108–119. https://doi.org/https://doi.org/10.1016/j.bbagen.2015.09.012.

(7) Barenholz, Y. (Chezy). Doxil® — The First FDA-Approved Nano-Drug: Lessons Learned. *J. Control. Release* **2012**, *160* (2), 117–134. https://doi.org/https://doi.org/10.1016/j.jconrel.2012.03.020.

(8) Grasianto; Fukuyama, M.; Mott, D. M.; Koseki, Y.; Kasai, H.; Hibara, A. Organic Nanocrystal Enrichment in Paper Microfluidic Analysis. *Sensors Actuators B Chem.* **2021**, *333*, 129548. https://doi.org/https://doi.org/10.1016/j.snb.2021.129548.

(9) Jiang, H.; Hu, W. The Emergence of Organic Single-Crystal Electronics. *Angew. Chemie Int. Ed.* **2020**, *59* (4), 1408–1428. https://doi.org/https://doi.org/10.1002/anie.201814439.

(10) Sanz, N.; Ibanez, A.; Morel, Y.; Baldeck, P. L. Organic Nanocrystals Grown in Gel Glasses for Optical-Power-Limiting Applications. *Appl. Phys. Lett.* **2001**, *78* (17), 2569–2571. https://doi.org/10.1063/1.1364660.

(11) Yan, X.; Remond, M.; Zheng, Z.; Hoibian, E.; Soulage, C.; Chambert, S.; Andraud, C.; Van der Sanden, B.; Ganachaud, F.; Bretonnière, Y.; Bernard, J. General and Scalable Approach to Bright, Stable, and Functional AIE Fluorogen Colloidal Nanocrystals for in Vivo Imaging. *ACS Appl. Mater. Interfaces* **2018**, *10* (30), 25154–25165. https://doi.org/10.1021/acsami.8b07859.

(12) Fateminia, S. M. A.; Wang, Z.; Liu, B. Nanocrystallization: An Effective Approach to Enhance the Performance of Organic Molecules. *Small Methods* **2017**, *1* (3), 1600023-n/a. https://doi.org/10.1002/smtd.201600023.

(13) Fateminia, S. M. A.; Mao, Z.; Xu, S.; Yang, Z.; Chi, Z.; Liu, B. Organic Nanocrystals with Bright Red Persistent Room-Temperature Phosphorescence for Biological Applications. *Angew. Chemie Int. Ed.* **2017**, *56* (40), 12160–12164. https://doi.org/https://doi.org/10.1002/anie.201705945.

(14) Fateminia, S. M. A.; Wang, Z.; Goh, C. C.; Manghnani, P. N.; Wu, W.; Mao, D.; Ng, L. G.; Zhao, Z.; Tang, B. Z.; Liu, B. Nanocrystallization: A Unique Approach to Yield Bright Organic Nanocrystals for Biological Applications. *Adv. Mater.* **2017**, *29* (1), 1604100. https://doi.org/10.1002/adma.201604100.

(15) Qu, X.; Li, Y.; Li, L.; Wang, Y.; Liang, J.; Liang, J. Fluorescent Gold Nanoclusters: Synthesis and Recent Biological Application. *J. Nanomater.* **2015**, *2015*. https://doi.org/10.1155/2015/784097.

(16) Fery-Forgues, S. Fluorescent Organic Nanocrystals and Non-Doped Nanoparticles for Biological Applications. *Nanoscale* **2013**, *5* (18), 8428–8442. https://doi.org/10.1039/C3NR02657D.

(17) Mei, J.; Leung, N. L. C.; Kwok, R. T. K.; Lam, J. W. Y.; Tang, B. Z. Aggregation-Induced Emission: Together We Shine, United We Soar! *Chem. Rev.* **2015**, *115* (21), 11718–11940. https://doi.org/10.1021/acs.chemrev.5b00263.

(18) Qian, J.; Wang, D.; He, S. Aggregation-Induced Emission Dyes for In Vivo Functional Bioimaging. In *Aggregation-Induced Emission: Fundamentals and Applications, Volumes 1 and 2*; John Wiley & Sons, Ltd, 2013; pp 209–237. https://doi.org/https://doi.org/10.1002/9781118735183.ch28.

(19) Rosendale, M.; Flores, J.; Paviolo, C.; Pagano, P.; Daniel, J.; Ferreira, J.; Verlhac, J.-B.; Groc, L.; Cognet, L.; Blanchard-Desce, M. A Bottom-Up Approach to Red-Emitting Molecular-Based Nanoparticles with Natural Stealth Properties and Their Use for Single-Particle Tracking Deep in Brain Tissue. *Adv. Mater.* **2021**, *33* (22), 2006644. https://doi.org/https://doi.org/10.1002/adma.202006644.

(20) Evrard, Q.; Houard, F.; Daiguebonne, C.; Calvez, G.; Suffren, Y.; Guillou, O.; Mannini, M.; Bernot, K. Sonocrystallization as an Efficient Way to Control the Size, Morphology, and Purity of Coordination Compound Microcrystallites: Application to a Single-Chain Magnet. *Inorg. Chem.* **2020**, *59* (13), 9215–9226.

https://doi.org/10.1021/acs.inorgchem.0c01126.

(21) Jordens, J.; Gielen, B.; Xiouras, C.; Hussain, M. N.; Stefanidis, G. D.; Thomassen, L. C. J.; Braeken, L.; Van Gerven, T. Sonocrystallisation: Observations, Theories and Guidelines. *Chem. Eng. Process. - Process Intensif.* **2019**, *139*, 130–154. https://doi.org/https://doi.org/10.1016/j.cep.2019.03.017.

(22) Luque de Castro, M. D.; Priego-Capote, F. Ultrasound-Assisted Crystallization (Sonocrystallization). *Ultrason. Sonochem.* **2007**, *14* (6), 717–724. https://doi.org/https://doi.org/10.1016/j.ultsonch.2006.12.004.

(23) LaMer, V. K.; Dinegar, R. H. Theory, Production and Mechanism of Formation of Monodispersed Hydrosols. *J. Am. Chem. Soc.* **1950**, *72* (11), 4847–4854. https://doi.org/10.1021/ja01167a001.

(24) Murray, C. B.; Kagan, C. R.; Bawendi, M. G. Synthesis and Characterization of Monodisperse Nanocrystals and Close-Packed Nanocrystal Assemblies. *Annu. Rev. Mater. Sci.* **2000**, *30* (1), 545–610. https://doi.org/10.1146/annurev.matsci.30.1.545.

(25) Sanz, N.; Baldeck, P. L.; Ibanez, A. Organic Nanocrystals Embedded in Sol–Gel Glasses for Optical Applications. *Synth. Met.* **2000**, *115* (1), 229–234. https://doi.org/https://doi.org/10.1016/S0379-6779(00)00340-4.

(26) Sanz, N.; Baldeck, P. L.; Nicoud, J.-F.; Le Fur, Y.; Ibanez, A. Polymorphism and Luminescence Properties of CMONS Organic Crystals: Bulk Crystals and Nanocrystals Confined in Gel-Glasses. *Solid State Sci.* **2001**, *3* (8), 867–875. https://doi.org/https://doi.org/10.1016/S1293-2558(01)01192-X.

(27) Vrcelj, R. M.; Shepherd, E. E. A.; Yoon, C.-S.; Sherwood, J. N.; Kennedy, A. R. Preparation and Structural Evaluation of the Conformational Polymorphs of α-[(4-Methoxyphenyl)Methylene]-4-Nitrobenzeneacetonitrile. *Cryst. Growth Des.* **2002**, *2* (6), 609–617. https://doi.org/10.1021/cg025529h.

(28) Philippot, C.; Zimmermann, J.; Dubois, F.; Bacia, M.; Boury, B.; Baldeck, P. L.; Brasselet, S.; Ibanez, A. Polymorphism of CMONS Nanocrystals Grown in Silicate Particles through a Spray-Drying Process. *Cryst. Growth Des.* **2013**, *13* (12), 5241–5248. https://doi.org/10.1021/cg401000t.

(29) Merckx, R. Sur Quelques Produits de Condensation de Systèmes à Méthylène Actif Avec Les Aldéhydes. *Bull. des Sociétés Chim. Belges* **1949**, *58* (10-12), 460–471. https://doi.org/https://doi.org/10.1002/bscb.19490581005.

(30) Mentink-Vigier, F.; Marin-Montesinos, I.; Jagtap, A. P.; Halbritter, T.; van Tol, J.; Hediger, S.; Lee, D.; Sigurdsson, S. T.; De Paëpe, G. Computationally Assisted Design of Polarizing Agents for Dynamic Nuclear Polarization Enhanced NMR: The AsymPol Family. *J. Am. Chem. Soc.* **2018**, *140* (35), 11013–11019. https://doi.org/10.1021/jacs.8b04911.

(31) Rosay, M.; Blank, M.; Engelke, F. Instrumentation for Solid-State Dynamic Nuclear Polarization with Magic Angle Spinning NMR. *J. Magn. Reson.* **2016**, *264*, 88–98. https://doi.org/10.1016/j.jmr.2015.12.026.

(32) Stejskal, E. O.; Schaefer, J.; Waugh, J. S. Magic-Angle Spinning and Polarization Transfer in Proton-Enhanced NMR. *J. Magn. Reson.* **1977**, *28* (1), 105–112. https://doi.org/10.1016/0022-2364(77)90260-8.

(33) Pines, A.; Gibby, M. G.; Waugh, J. S. Proton-Enhanced NMR of Dilute Spins in Solids. *J. Chem. Phys.* **1973**, *569* (1973), 569–590. https://doi.org/10.1063/1.1680061.

(34) Metz, G.; Wu, X. L.; Smith, S. O. Ramped-Amplitude Cross Polarization in Magic-Angle-Spinning NMR. *J. Magn. Reson. Ser. A* **1994**, *110* (2), 219–227. https://doi.org/10.1006/jmra.1994.1208.

(35) Hediger, S.; Meier, B. H.; Ernst, R. R. Cross Polarization under Fast Magic Angle Sample Spinning Using Amplitude-Modulated Spin-Lock Sequences. *Chem. Phys. Lett.* **1993**, *213* (5–6), 627–635. https://doi.org/10.1016/0009-2614(93)89172-E.

(36) Hediger, S.; Meier, B. H.; Kurur, N. D.; Bodenhausen, G.; Ernst, R. R. NMR Cross Polarization by Adiabatic Passage through The. *Chem. Phys. Lett.* **1994**, *223* (June), 283–288.

(37) Fung, B. M.; Khitrin, A. K.; Ermolaev, K. V. An Improved Broadband Decoupling Sequence for Liquid Crystals and Solids. *J. Magn. Reson.* **2000**, *142 1*, 97–101.

(38) Monnier, V.; Sanz, N.; Botzung-Appert, E.; Bacia, M.; Ibanez, A. Confined Nucleation and Growth of Organic Nanocrystals in Sol-Gel Matrices. *J. Mater. Chem.* **2006**, *16* (15), 1401–1409. https://doi.org/10.1039/B509833P.

(39) Mason, T. J. Some Neglected or Rejected Paths in Sonochemistry – A Very Personal View. *Ultrason. Sonochem.* **2015**, *25*, 89–93. https://doi.org/https://doi.org/10.1016/j.ultsonch.2014.11.014.

(40) Yao, J. H.; Chen, Y.; Pang, Y. Application of Sonochemistry in the Isomerization of Carbon-Carbon Double Bonds. *J. Polym. Sci. Part A Polym. Chem.* **2010**, *48* (22), 5254–

5257. https://doi.org/10.1002/pola.24301.

(41) Shenoi-Perdoor, S.; Cattoën, X.; Bretonnière, Y.; Eucat, G.; Andraud, C.; Gennaro, B.; Kodjikian, S.; Dubois, F.; Ibanez, A. Red-Emitting Fluorescent Organic@silicate Core–Shell Nanoparticles for Bio-Imaging. *New J. Chem.* **2018**, *42* (18), 15353–15360. https://doi.org/10.1039/C8NJ03297A.

(42) Cai, Z.; Wu, Y.; Chen, S. Energy-Dependent Knock-on Damage of Organic–Inorganic Hybrid Perovskites under Electron Beam Irradiation: First-Principles Insights. *Appl. Phys. Lett.* **2021**, *119* (12), 123901. https://doi.org/10.1063/5.0065849.

(43) Gerfen, G. J.; Becerra, L. R.; Hall, D. A.; Griffin, R. G.; Temkin, R. J.; Singel, D. J. High Frequency (140 GHz) Dynamic Nuclear Polarization: Polarization Transfer to a Solute in Frozen Aqueous Solution. *J. Chem. Phys.* **1995**, *102* (24), 9494–9497. https://doi.org/10.1063/1.468818.

(44) Lee, D.; Hediger, S.; Paëpe, G. De. High-Field Solid-State NMR with Dynamic Nuclear Polarization BT - Modern Magnetic Resonance; Webb, G. A., Ed.; Springer International Publishing: Cham, 2018; pp 861–877. https://doi.org/10.1007/978-3-319-28388-3_73.

(45) van der Wel, P. C. A.; Hu, K.-N.; Lewandowski, J.; Griffin, R. G. Dynamic Nuclear Polarization of Amyloidogenic Peptide Nanocrystals: GNNQQNY, a Core Segment of the Yeast Prion Protein Sup35p. *J. Am. Chem. Soc.* **2006**, *128* (33), 10840–10846. https://doi.org/10.1021/ja0626685.

(46) Pinon, A. C.; Rossini, A. J.; Widdifield, C. M.; Gajan, D.; Emsley, L. Polymorphs of Theophylline Characterized by DNP Enhanced Solid-State NMR. *Mol. Pharm.* **2015**, *12*

(11), 4146–4153. https://doi.org/10.1021/acs.molpharmaceut.5b00610.

(47) Gutmann, T.; Liu, J.; Rothermel, N.; Xu, Y.; Jaumann, E.; Werner, M.; Breitzke, H.; Sigurdsson, S. T.; Buntkowsky, G. Natural Abundance 15N NMR by Dynamic Nuclear Polarization: Fast Analysis of Binding Sites of a Novel Amine-Carboxyl-Linked Immobilized Dirhodium Catalyst. *Chem. – A Eur. J.* **2015**, *21* (9), 3798–3805. https://doi.org/https://doi.org/10.1002/chem.201405043.

(48) Märker, K.; Pingret, M.; Mouesca, J.-M.; Gasparutto, D.; Hediger, S.; De Paëpe, G. A New Tool for NMR Crystallography: Complete 13C/15N Assignment of Organic Molecules at Natural Isotopic Abundance Using DNP-Enhanced Solid-State NMR. *J. Am. Chem. Soc.* **2015**, *137* (43), 13796–13799. https://doi.org/10.1021/jacs.5b09964.

(49) Mollica, G.; Dekhil, M.; Ziarelli, F.; Thureau, P.; Viel, S. Quantitative Structural Constraints for Organic Powders at Natural Isotopic Abundance Using Dynamic Nuclear Polarization Solid-State NMR Spectroscopy. *Angew. Chem. Int. Ed. Engl.* **2015**, *54* (20), 6028–6031. https://doi.org/10.1002/anie.201501172.

(50) Veinberg, S. L.; Johnston, K. E.; Jaroszewicz, M. J.; Kispal, B. M.; Mireault, C. R.; Kobayashi, T.; Pruski, M.; Schurko, R. W. Natural Abundance 14N and 15N Solid-State NMR of Pharmaceuticals and Their Polymorphs. *Phys. Chem. Chem. Phys.* **2016**, *18* (26), 17713–17730. https://doi.org/10.1039/C6CP02855A.

(51) Zhao, L.; Pinon, A. C.; Emsley, L.; Rossini, A. J. DNP-Enhanced Solid-State NMR Spectroscopy of Active Pharmaceutical Ingredients. *Magn. Reson. Chem.* **2018**, *56* (7), 583–609. https://doi.org/10.1002/mrc.4688.

(52) Smith, A. N.; Märker, K.; Hediger, S.; De Paëpe, G. Natural Isotopic Abundance 13C and 15N Multidimensional Solid-State NMR Enabled by Dynamic Nuclear Polarization. *J. Phys. Chem. Lett.* **2019**, *10* (16), 4652–4662. https://doi.org/10.1021/acs.jpclett.8b03874.

(53) Gutmann, T.; Groszewicz, P. B.; Buntkowsky, G. Solid-State NMR of Nanocrystals. *Annu. Reports NMR Spectrosc.* **2019**, *97*, 1–82. https://doi.org/https://doi.org/10.1016/BS.ARNMR.2018.12.001.

(54) Kumar, A.; Durand, H.; Zeno, E.; Balsollier, C.; Watbled, B.; Sillard, C.; Fort, S.; Baussanne, I.; Belgacem, N.; Lee, D.; Hediger, S.; Demeunynck, M.; Bras, J.; De Paëpe, G. The Surface Chemistry of a Nanocellulose Drug Carrier Unravelled by MAS-DNP. *Chem. Sci.* **2020**, *11* (15), 3868–3877. https://doi.org/10.1039/C9SC06312A.

(55) Earl, W. L.; Vanderhart, D. L. Observations by High-Resolution Carbon-13 Nuclear Magnetic Resonance of Cellulose I Related to Morphology and Crystal Structure. *Macromolecules* **1981**, *14*, 570–574. https://doi.org/https://doi.org/10.1021/ma50004a023.

(56) Alla, M.; Lippmaa, E. Resolution Limits in Magic-Angle Rotation NMR Spectra of Polycrystalline Solids. *Chem. Phys. Lett.* **1982**, *87* (1), 30–33. https://doi.org/https://doi.org/10.1016/0009-2614(82)83547-1.

(57) Barich, D. H.; Davis, J. M.; Schieber, L. J.; Zell, M. T.; Munson, E. J. Investigation of Solid-State NMR Line Widths of Ibuprofen in Drug Formulations. *J. Pharm. Sci.* **2006**, *95 7*, 1586–1594. https://doi.org/https://doi.org/10.1002/JPS.20564.

(58) Hanrahan, M. P.; Venkatesh, A.; Carnahan, S. L.; Calahan, J. L.; Lubach, J. W.; Munson, E. J.; Rossini, A. J. Enhancing the Resolution of 1H and 13C Solid-State NMR Spectra by

Reduction of Anisotropic Bulk Magnetic Susceptibility Broadening. *Phys. Chem. Chem. Phys.* **2017**, *19* (41), 28153–28162. https://doi.org/10.1039/C7CP04223J.

(59) Eucat, G. Ingénierie Moléculaire de Nouveaux Émetteurs à l’état Solide et Élaboration de Nanoparticules Coeurcoquilles Pour l’imagerie Médicale, Université de Grenoble, 2014.

(60) Zhang, Z.; Sun, H.; Shao, X.; Li, D.; Yu, H.; Han, M. Three-Dimensionally Oriented Aggregation of a Few Hundred Nanoparticles into Monocrystalline Architectures. *Adv. Mater.* **2005**, *17* (1), 42–47. https://doi.org/https://doi.org/10.1002/adma.200400401.

(61) Rodriguez-Liviano, S.; Aparicio, F. J.; Rojas, T. C.; Hungría, A. B.; Chinchilla, L. E.; Ocaña, M. Microwave-Assisted Synthesis and Luminescence of Mesoporous RE-Doped YPO4 (RE = Eu, Ce, Tb, and Ce + Tb) Nanophosphors with Lenticular Shape. *Cryst. Growth Des.* **2012**, *12* (2), 635–645. https://doi.org/10.1021/cg201358c.

(62) Ramanujam, P.; Vaidhyanathan, B.; Binner, J. G. P.; Ghanizadeh, S.; Spacie, C. Solvothermal NanoYAG Synthesis: Mechanism and Particle Growth Kinetics. *J. Supercrit. Fluids* **2016**, *107*, 433–440. https://doi.org/https://doi.org/10.1016/j.supflu.2015.09.031.

(63) Roose, B.; Ummadisingu, A.; Correa-Baena, J.-P.; Saliba, M.; Hagfeldt, A.; Graetzel, M.; Steiner, U.; Abate, A. Spontaneous Crystal Coalescence Enables Highly Efficient Perovskite Solar Cells. *Nano Energy* **2017**, *39*, 24–29. https://doi.org/https://doi.org/10.1016/j.nanoen.2017.06.037.

For Table of Contents Use Only

Sonocrystallization of CMONS needles and nanocubes: mechanistic studies and advanced crystallinity characterizations by combining X-ray and electron diffractions with DNP-enhanced NMR

Cattoën, Xavier; Kumar, Akshay; Dubois, Fabien; Matta-Seclén, Mauricio; Vaillant, Carole; Leynaud, Olivier; Kodjikian, Stéphanie; Hediger, Sabine; De Paëpe, Gaël; Ibanez, Alain

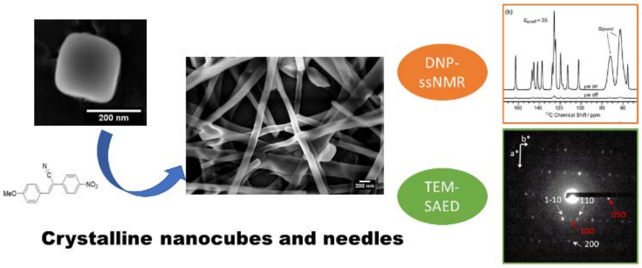

Ultrasound-assisted nanocrystallization of the CMONS dye afforded nanocubes or needles which crystallinity was assessed by PXRD, electron diffraction, DNP-enhanced solid-state NMR and fluorescence quantum yield measurements.